# Reduced-cost supercell approach for computing accurate phonon density of states in organic crystals

Cameron Cook<sup>1</sup> and Gregory J. O. Beran<sup>1, a)</sup>

Department of Chemistry, University of California, Riverside, California 92521, United States

(Dated: 13 November 2020)

Phonon contributions to organic crystal structures and thermochemical properties can be significant, but computing a well-converged phonon density of states with lattice dynamics and periodic density functional theory (DFT) is often computationally expensive due to the need for large supercells. Using semi-empirical methods like density functional tight binding (DFTB) instead of DFT can reduce the computational costs dramatically, albeit with noticeable reductions in accuracy. This work proposes approximating the phonon density of states via a relatively inexpensive DFTB supercell treatment of the phonon dispersion that is then corrected by shifting the individual phonon modes according to the difference between the DFT and DFTB phonon frequencies at the Γ-point. The acoustic modes are then computed at the DFT level from the elastic constants. In several small-molecule crystal test cases, this combined approach reproduces DFT thermochemistry with kJ/mol accuracy and 1–2 orders of magnitude less computational effort. Finally, this approach is applied to computing the free energy differences between the five crystal polymorphs of oxalyl dihydrazide.

a) Electronic mail: gregory.beran@ucr.edu

## I. INTRODUCTION

Organic molecular crystals are prevalent in pharmaceuticals, organic semiconductors, energetic materials, and many other organic materials. Different crystal packings of a given molecule, known as polymorphs, can exhibit distinct physical properties, such as stability, solubility or charge-carrier mobility. Knowledge of the different possible polymorphs and their relative stabilities, called the crystal energy landscape, can be valuable for designing new materials with specific properties. However, reliable prediction of crystal energy landscapes is hindered by the small, few kJ/mol or less free energy differences that often separate different polymorphs.<sup>1–3</sup> Further complications arise from how those relative thermochemical stabilities can vary with temperature and pressure.<sup>4</sup> Accurate computational models are often required to map out these solid form landscapes correctly.<sup>5–9</sup>

Polymorph free energies are dominated by the electronic lattice energy contribution. Indeed, lattice energy rankings have long been the primary metric employed when ranking predicted crystal structures.<sup>5,10,11</sup> However, it is also clear that the vibrational contributions to the free energy can be important. Surveys suggest that  $F_{vib}$  contributions are sufficiently large to reverse the lattice energy stability orderings in 10–20% of polymorphic systems at room temperature.<sup>1,12</sup> Phonon contributions are crucial to understanding why aspirin form I is thermodynamically preferred over form II,<sup>13</sup> and they have proved necessary to predict the thermodynamically most stable polymorphs correctly for several molecules in the blind tests of crystal structure prediction.<sup>6,7</sup>

More elaborate quasi-harmonic phonon treatments describe how the crystal structure and phonon frequencies change with temperature and pressure. Accounting for these changes is important for predicting properties including lattice parameters/molar volumes, <sup>14–16</sup> thermochemical properties, <sup>14,15,17–21</sup> mechanical properties, <sup>22,23</sup> vibrational spectra, <sup>24,25</sup> and nuclear magnetic resonance chemical shifts. <sup>26</sup> Capturing those pressure- and temperature-dependent changes in thermochemical properties proved essential to predicting the phase diagram of methanol, for example. <sup>20</sup> Beyond harmonic or quasi-harmonic treatments, there is increasing evidence that dynamics plays an important role in the structures and thermochemical stabilities of molecular crystals. <sup>27–30</sup>

Unfortunately, even within the harmonic approximation, computing a well-converged phonon density of states for a chemically interesting organic crystal can be very computationally demanding. The most straightforward approach to computing harmonic phonon modes relies on lattice dynamical calculations performed in large supercells to capture phonon dispersion.<sup>31</sup> Typically, the supercell should extend 10–15 Å in each direction,<sup>32,33</sup> and it will often contain hundreds of atoms. Density functional perturbation theory avoids the need for supercells and can compute the phonons at lower cost,<sup>34</sup> but the calculations remain computationally demanding.

One means of reducing the computational costs associated with evaluating the harmonic phonon density of states (pDOS) and the vibrational partition functions is to compute the phonons at a lower level of theory. For example, the use of DFT-optimized geometries and phonon frequencies together with single-point energies computed via correlated wave function methods has proved effective.<sup>35</sup>

Alternatively, some researchers have explored the use of computationally inexpensive density functional tight binding (DFTB) models for predicting the structures and phonons. DFTB is a semi-empirical quantum mechanical method that is based off of the generalized gradient approximation (GGA) of DFT.<sup>36,37</sup> It expresses the electronic energy as a Taylor expansion about a reference DFT electron density  $\rho_0$ . The present work focuses on DFTB3, which includes terms through third-order in the expansion.<sup>38</sup> For systems like molecular crystals in which non-covalent interactions are important, DFTB3 must be paired with a dispersion correction, such as Grimme's D3 model.<sup>39</sup> Hydrogen bonding corrections can provide further improvements.<sup>40</sup> The combination of a minimal basis set of Slater-type orbitals and semi-empirical parameterization speeds DFTB by up to three orders of magnitude over ab initio DFT.

In the context of molecular crystals, DFTB has proved effective for optimizing crystal structures,<sup>41</sup> and it predicts the thermal expansion in carbamazepine accurately.<sup>42</sup> It can provide useful intermediate rankings of crystal structures in a multi-step, hierarchical crystal structure prediction,<sup>43</sup> and it can provide good embedding environment for DFT.<sup>44</sup> On the other hand, existing DFTB approximations and parameterizations appear insufficiently accurate for the final ranking stages of crystal structure prediction.<sup>43,45–48</sup> On the X23 benchmark set of molecular crystals, for example, it exhibits a mean absolute deviation in the lattice energies of 10 kJ/mol, compared to 5–6 kJ/mol for many dispersion-corrected GGA density functionals.<sup>45,46</sup> As the data presented below will demonstrate, DFTB performance is often noticeably worse than DFT for computing the phonon density of states and

the thermochemical properties derived from it.

Here, we propose a strategy for computing the harmonic pDOS that combines the computational efficiency of DFTB with the greater accuracy of DFT. In this approach, a supercell harmonic phonon calculation is performed at the dispersion-corrected DFTB3 level to capture the phonon dispersion, which is far more affordable than GGA DFT. However, the limitations of DFTB semi-empirical parameterizations mean that there will often be sizable errors in the phonon frequencies. Therefore, an additional  $\Gamma$ -point harmonic phonon frequency calculation is performed on the crystallographic unit cell with DFT. By matching the  $\Gamma$ -point modes between DFT and DFTB, we determine an additive offset for each individual DFTB phonon frequency that enables shifting of the DFTB dispersion curves such that they agree exactly with DFT at the  $\Gamma$  point. This simple shift improves the agreement between the low-cost DFTB and full DFT pDOS considerably. This corrected DFTB pDOS can be computed at least 1–2 orders of magnitude faster than the full supercell DFT calculation while sacrificing only modest accuracy in the final predicted thermochemical properties. Although the present study focuses purely on a harmonic phonon description, the generalization of the ideas here to a quasi-harmonic treatment for the more reliable treatment of temperature-dependent effects would be straightforward.

# II. THEORY

## A. Approximating the phonon density of states

The principal finite-temperature contributions to the Gibbs free energy of a crystal arise from the Helmholtz vibrational energy,  $F_{vib}(T)$ . From statistical thermodynamics and the harmonic approximation, one obtains,

$$F_{vib}(T) = 3nN_A k_B T \int_0^\infty \ln\left[2\sinh\left(\frac{\hbar\omega}{2k_B T}\right)\right] g(\omega) d\omega \tag{1}$$

where n is the number of atoms in the unit cell,  $N_A$  is Avogadro's number,  $g(\omega)$  is the phonon density of states as a function of frequency  $\omega$ ,  $\hbar$  is Planck's constant,  $k_B$  is the Boltzman constant, and T is temperature.<sup>49</sup> The density of states  $g(\omega)$  is normalized to unity (hence the factor of 3n in Eq 1) and is expressed as a kernel density estimate (KDE) of the overall frequency distribution for all phonon modes  $\omega_i$  and all  $\mathbf{k}$  by placing primitive Gaussian

functions of width 5 cm<sup>-1</sup> at each discrete phonon mode about each sampled k-point. Use of the KDE improves the convergence of thermodynamic properties with respect to phonon sampling.<sup>12</sup>

To evaluate the phonon dispersion in reciprocal space that contributes to the phonon density of states, it is necessary to generate a supercell consisting of multiple crystallographic unit cells in order to describe how the phonon frequency changes with respect to its interaction with neighboring cells. Doing so often dramatically increases the size of the system to be modeled and can make the computational cost prohibitive with DFT or other *ab initio* methods. The complexity introduced by phonon dispersion is often circumvented by simply evaluating the frequencies at the  $\Gamma$ -point (zone center,  $\mathbf{k} = \mathbf{0}$ ) of the unit cell, which can be accomplished without supercell expansion. However, this  $\Gamma$ -point-only approximation omits potentially important contributions to the pDOS from the acoustic modes and dispersion of the optical modes away from the zone center.

Before describing the proposed efficient approach for computing the pDOS, the theory of lattice dynamics will be reviewed briefly. Within the harmonic approximation, the crystal potential can be approximated via the second term of the Taylor expansion of overall potential with respect to atomic displacements,

$$V = V_0 + \sum_{l,\alpha} V_{\alpha}^l u_{\alpha}^l + \frac{1}{2} \sum_{l,l',\alpha,\beta} V_{\alpha\beta}^{ll'} u_{\alpha}^l u_{\beta}^{l'} + \cdots$$
 (2)

$$V_{\alpha\beta}^{ll'} = \frac{\partial^2 V}{\partial u_{\alpha}^l \partial u_{\beta}^{l'}} \tag{3}$$

where V is crystal potential and  $u_{\alpha}^{l}$  is the displacement of atom l in direction  $\alpha$ .  $V_{\alpha}^{l}$  represents the nuclear gradient of the potential with respect to the displacement of atom l, which equals zero when the structure has been optimized to a stationary point.  $V_{\alpha\beta}^{ll'}$  is the matrix of force constants describing the forces felt by atom l in the central unit cell after the displacement of atom l'. Mass weighting and transforming the coordinates into reciprocal space yields the dynamical matrix  $D_{\alpha\beta}$ , which can be diagonalized according to:

$$\omega^2 u_{\alpha} = \sum_{\beta} D_{\alpha\beta} u_{\beta} \quad \text{where} \quad D_{\alpha\beta} = \frac{1}{\sqrt{m_l m_{l'}}} \sum_{n} V_{\alpha,\beta}^{l,l'} \exp(-i\mathbf{k} \cdot \mathbf{r}_n)$$
 (4)

This dynamical matrix equation relates atomic displacement, force response, and resulting vibrational frequencies  $\omega$ . The normal mode eigenvectors  $u_{\alpha}$  are normalized vectors describing the collective movement of the atoms that result in the frequency of that mode.

The hybrid approach proposed here seeks to benefit from the low-computational cost of DFTB while mitigating its comparatively lower accuracy. In particular, we capture phonon dispersion via large supercell DFTB calculations. The low-cost of DFTB makes it more feasible to converge the pDOS with respect to supercell size. To address the accuracy limitations of the DFTB pDOS, an additive correction is applied to the frequencies associated with each DFTB phonon mode. This shift is computed separately for each mode i as the difference between the DFT and DFTB frequencies at the  $\Gamma$ -point,

$$\omega_i^{final}(\mathbf{k}) \approx \omega_i^{DFTB}(\mathbf{k}) + (\omega_i^{DFT}(\mathbf{\Gamma}) - \omega_i^{DFTB}(\mathbf{\Gamma}))$$
 (5)

Performing this frequency shift does require computing the DFT frequencies at the  $\Gamma$  point, which is far more expensive than computing them with DFTB for the same unit cell. On the other hand, the cost of the DFT  $\Gamma$ -point calculation can be orders of magnitude cheaper than computing the DFT frequencies in a large supercell. Overall, this simple correction approximates the DFT phonon density of states well at a fraction of the usual computational cost.

The approximation in Eq 5 assumes that the dispersion in individual phonon bands is similar regardless of whether they are computed with DFT or DFTB, and that the simple additive correction is sufficient to improve the DFTB bands. That assumption is imperfect—our own anecdotal examinations of the pDOS for a few systems suggest that the DFTB3-D3(BJ) bands with the 3ob-3-1 parameter set<sup>51</sup> tend to exhibit greater frequency dispersion across the Brillouin zone compared to their B86bPBE-XDM DFT counterparts. Nevertheless, these discrepancies in individual phonon bands partially cancel in the total pDOS, and the correction improves the overall phonon density of states considerably compared to the target DFT calculations. Note too that this  $\Gamma$ -point shift does not work for the three acoustic modes, since those phonon frequencies equal zero at  $\mathbf{k} = \mathbf{0}$ , regardless of the electronic structure treatment. The acoustic modes will be handled separately, as described in Section II B.

Employing this proposed hybrid pDOS calculation strategy requires addressing a few practical issues. First, the harmonic approximation requires that the crystal structure has been relaxed to an energy minimum at the same level of theory as the lattice dynamics calculation. Accordingly, the crystal geometry is first optimized with DFT for the  $\Gamma$ -point phonon calculation. The DFT-optimized unit cell is then relaxed with DFTB for the supercell lattice

dynamics calculation.

Second, applying Eq 5 requires identifying which DFT phonon modes correspond to which DFTB modes. Due to differences in the optimized structures and the electronic structure models, the phonon frequencies will differ both in magnitude and the ordering obtained from the eigenvalue solver. The normal mode eigenvectors obtained from diagonalizing the  $\Gamma$ -point dynamical matrix (Eq 4) at each level of theory will also likely differ quantitatively, though they should still correspond to qualitatively similar atomic motions. Therefore, to match phonon normal modes between the two levels of theory, the overlap matrix  $\langle u_{\alpha}^{DFTB}(\Gamma)|u_{\beta}^{DFT}(\Gamma)\rangle$  is computed as the set of all possible inner products between the DFT and DFTB normal modes at the  $\Gamma$ -point. The optimal mode match for each DFT normal mode is then assigned based on the single largest overlapping DFTB normal mode eigenvector (with each DFTB mode being allowed to match only one DFT mode).

Figure 1 plots a sample overlap matrix for the DFT (B86bPBE-XDM) and DFTB3-D3(BJ) normal mode eigenvectors of phase I carbon dioxide at the Γ-point (see Section III for computational details). With only 12 atoms in the unit cell and 33 normal modes (excluding the acoustic modes), the overlap matrix can be visualized easily. For the vast majority of modes, there exists a single, clear match between the two levels of theory. The degree of the overlap can be smaller for degenerate modes, since the corresponding eigenvectors are not unique. However, this does not present a problem in practice as long as the correct subspaces are identified, since individual assignments within the subspace are arbitrary. Once the DFTB bands have been fully assigned, they can be shifted according to Eq 5 to construct the final approximate pDOS.

The overlap-based mode assignment has proved straightforward for all systems studied thus far. It is conceivable that one might find a system for which the simpler DFTB model performs poorly and for which assigning the modes becomes more difficult. As the DFTB models and parameterizations are continually improved, however, the likelihood of such difficulties will hopefully decrease even further.

# B. Treatment of the acoustic modes

As noted above, the  $\Gamma$ -point shift cannot be applied to the three acoustic modes, since those frequencies equal zero at the  $\Gamma$  point by definition, regardless of the model chemistry

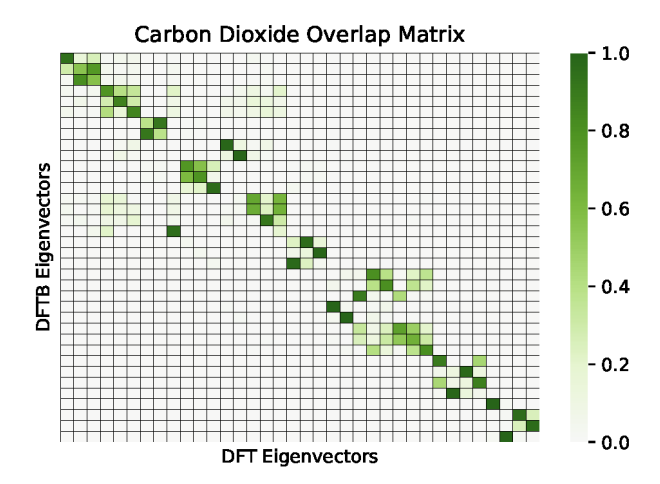


FIG. 1. Sample normal mode overlap matrix computed between the DFTB3-D3(BJ) and DFT (B86bPBE-XDM) normal mode eigenvectors for phase I CO<sub>2</sub>. Darker green corresponds to a larger-magnitude overlap.

employed. Moreover, very large supercells are required to converge the acoustic modes, which can become computationally expensive even with DFTB. Finally, it is unclear how well DFTB will model the soft acoustic vibrations in molecular crystals, given that such interactions were not a focus of the parameterization.

Instead, the acoustic modes here are solved for separately with DFT via the stress-strain relationships from the theory of elasticity, <sup>52,53</sup>

$$T = \lambda E \tag{6}$$

where T and E are the stress and strain tensors respectively, and  $\lambda$  is the matrix of elastic constants describing the stress-strain relationship.

Acoustic sound velocities  $\nu$  are related to the elastic constants using the  $3 \times 3$  Christoffel matrices  $\Gamma_{ik}$  for each unique direction in the Brillouin zone. The eigenvalues of these matrices describe the velocity of sound propagating through the crystal, which is associated with the frequency of the acoustic phonons.

$$\det |\Gamma_{ik} - \rho \nu^2 \delta_{ik}| = 0 \tag{7}$$

Within the long wave approximation,<sup>52</sup> the eigenvalues  $\rho\nu_i$  can be related to the spring constant  $\beta_i$  via the lattice constant a,

$$\rho \nu_i^2 = \beta_i a_j \tag{8}$$

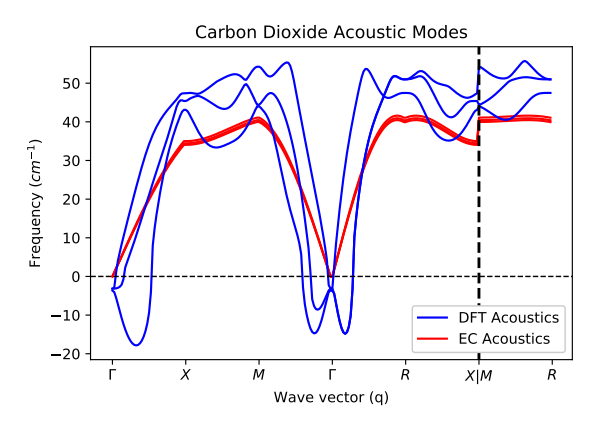


FIG. 2. Comparison of the acoustic phonon mode dispersion curves for crystalline carbon dioxide as computed directly from lattice dynamics (green)versus those derived from the elastic constants (red).

After averaging over the 13 unique Brillouin zone directions,<sup>54</sup> the final acoustic mode dispersion curves are computed as,

$$\omega = 2\sqrt{\frac{\bar{\beta}_i}{m}} \sin\left(\frac{ka_i}{2}\right) \tag{9}$$

where m is the mass of the unit cell and  $ka_i$  represents the position along a reciprocal space path. Once the acoustic mode dispersion has been evaluated, it is substituted in lieu of the DFTB acoustic modes in the final density of states.

Figure 2 plots the acoustic modes for phase I carbon dioxide as computed directly from DFT in a  $3 \times 3 \times 3$  supercell and from the elastic constant approach described above. Even in this 16.9 Å dimension supercell, the DFT acoustic modes retain significant imaginary components away from the  $\Gamma$  point. The elastic constant approach eliminates the imaginary components and broadly captures the k-point dependence of these modes, though the elastic constant model underestimates the frequencies by up to  $\sim 10$ –15 cm<sup>-1</sup> and exhibits reduced dispersion across the Brillouin zone. Nevertheless, the room-temperature Helmholtz vibrational free energies obtained from the acoustic mode contributions to the phonon density of states differ by only 0.2 kJ/mol between the two models.

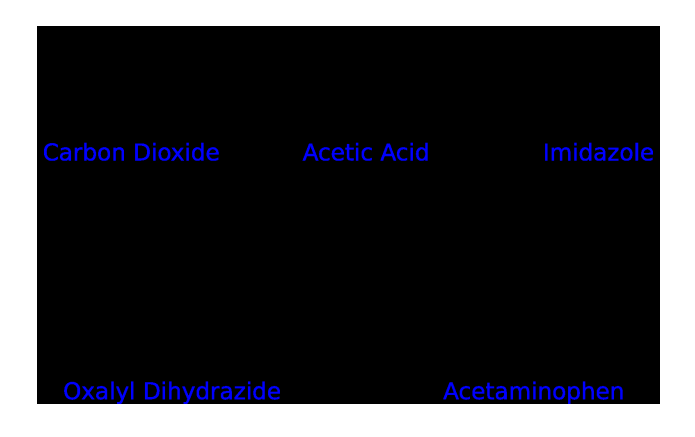


FIG. 3. The five species whose crystals are modeled here.

## III. COMPUTATIONAL METHODS

The atomic positions and lattice parameters of all crystals were fully relaxed starting from experimental crystal structures. The structure of carbon dioxide phase I was obtained from Ref. 55, while crystal structures of acetic acid (ACETAC01),<sup>56</sup> imidazole (IMAZOL06),<sup>57</sup> acetaminophen (HXACAN01),<sup>58</sup> and the five polymorphs of oxalyl dihydrazide (VIPKIO01–VIPKIO05)<sup>59</sup> were taken from the Cambridge Structural Database using the reference codes indicated in parentheses above. Molecular structures of these species are shown in Figure 3

The DFT geometry optimizations and finite displacements for the phonon calculations were performed using the B86bPBE density functional and the XDM dispersion correction, as implemented in Quantum Espresso v6.4.1.<sup>60</sup> The calculations employed a 40 Ry (acetic acid, due to the large supercell), 50 Ry (carbon dioxide, imidazole, and acetaminophen), or 60 Ry cutoff (oxalyl dihydrazide). Core electrons were treated according to the projector augmented wave (PAW) approach using PAW potentials for H, C, N, and O produced with A. Dal Corso's Atomic code v6.1. The DFTB3-D3 calculations were performed using the DFTB+ program<sup>61,62</sup> and the 3ob-3-1 Slater-Koster file parameter set.<sup>51</sup> Hubbard derivatives and empirical dispersion coefficients were set to the values recommended in the documentation.

For assessing the approximations proposed here, the specific choice of density functional and DFTB parameterization used to approximate the pDOS are somewhat arbitrary. The B86bPBE-XDM functional used here has performed well in many earlier molecular crystal studies.<sup>6,63–65</sup> Similarly, the dispersion-corrected DFTB3-D3(BJ) parameterization should also perform well for organic species like those studied here.<sup>51</sup> One might further improve

TABLE I. Supercell sizes used in the phonon calculations. Cells were chosen to achieve  $\sim 15$  Å or more in each direction, while also ensuring the supercell DFT calculations were feasible for the smaller molecules.

Crystal	Supercell	
Carbon Dioxide	$3\times3\times3$	
Acetic Acid	$2\times4\times3$	
Imidazole	$2 \times 3 \times 2$	
$\alpha$ Oxalyl Dihydrazide	$4 \times 3 \times 2$	
$\beta$ Oxalyl Dihydrazide	$5 \times 2 \times 3$	
$\gamma$ Oxalyl Dihydrazide	$4 \times 2 \times 3$	
$\delta$ Oxalyl Dihydrazide	$5 \times 2 \times 3$	
$\epsilon$ Oxalyl Dihydrazide	$3\times4\times2$	
Acetaminophen	$2 \times 2 \times 3$	

the quality of these models by switching to a hybrid density functional<sup>7,66</sup> or by including hydrogen bonding corrections in DFTB, for example.<sup>40</sup> Nevertheless, the results here focus primarily on how well the shifted DFTB pDOS reproduces the target DFT one and the impact of this on computed thermochemical properties, rather than carefully examining how well these particular DFT results reproduce experiment.

The harmonic phonon calculations were performed with Phonopy v1.13.2,<sup>67</sup> which generates a series of finite displacements in accord with the supercell/frozen phonon method. The DFT  $\Gamma$ -point calculations employ the relaxed crystallographic unit cell, while the DFTB phonon dispersion calculations employ a supercell constructed by replicating the unit cell after DFTB relaxation. To ensure good convergence of the force constants,<sup>50</sup> supercells were chosen to achieve dimensions of 15 Å or greater along each lattice vector. Table I lists the specific supercell sizes used. The dynamical matrix can then be diagonalized at various wave vectors  $\mathbf{k}$ . The  $\Gamma$ -point DFTB phonon frequencies used to match normal modes between DFT and DFTB are obtained at  $\mathbf{k} = \mathbf{0}$  from the supercell phonon calculation, while the remaining values at  $\mathbf{k} \neq \mathbf{0}$  provide the raw DFTB3-D3(BJ) pDOS. High-symmetry  $\mathbf{k}$  paths were assigned according to the schemes in Ref 68.

The matching of the phonon normal modes between DFT and DFTB and the elastic

constant solver algorithm were performed using in-house Python3 code. Elastic constants were solved in a similar manner to how they are implemented in Thermo\_PW module of the Quantum Espresso suite. <sup>69</sup> Thermo\_PW evaluates the elastic properties of a crystal by calculating the stress response for a series of strained conformations. Various magnitudes of each unique strain are applied, and the corresponding elastic constant is determined through a quadratic fit. Six unique stress/strain relationships are typically required to construct the elastic constant matrix, though this can often be simplified by exploiting crystal symmetry.

The stress/strain relationships were calculated via DFT. Test calculations found that DFTB3-D3(BJ) with the 3ob-3-1 parameterization gave elastic constants that differed considerably from the DFT ones. Performing these calculations with DFT instead of DFTB does not significantly increase the overall cost. The number of stress-strain relationships is independent of unit cell size, and evaluating each of the six stress-strain relationships involves four fixed-cell geometry optimizations of a slightly distorted crystallographic unit cell (rather than a supercell). All benchmark DFT phonon calculations here include the acoustic mode correction. To analyze how much this correction contributes, some DFTB results below include it, while others do not (as specified below).

#### IV. RESULTS AND DISCUSSION

To begin, Figure 4 compares the B86bPBE-XDM phonon density of states for the α polymorph of oxalyl dihydrazide against the DFTB3-D3(BJ) 3ob-3-1 ones before and after applying the Γ-point correction in Eq 5. These two models are referred to as "DFT" and "DFTB" for the remainder of the paper. For computational simplicity, the DFT and DFTB phonon dispersion calculations in this illustrative example employed only a 4×1×1 supercell (4×3×2 would be more appropriate for quantitative accuracy). As can be seen in Figure 4a, the raw DFTB pDOS differs noticeably from the DFT one. The discrepancies are most obvious in the intramolecular bends and stretches in the ~500-3500 cm<sup>-1</sup> range. For example, a number of the DFTB bending modes in the 540-595 cm<sup>-1</sup> range occur at 870–900 cm<sup>-1</sup> in the DFT pDOS. Considering all DFT phonon modes above 500 cm<sup>-1</sup>, the mean and mean absolute difference between DFT and DFTB are 54 and 84 cm<sup>-1</sup>, respectively. In other words, the DFTB model is systematically underestimating the bending and stretching frequencies on average. Discrepancies in higher-frequency intramolecular modes will primarily

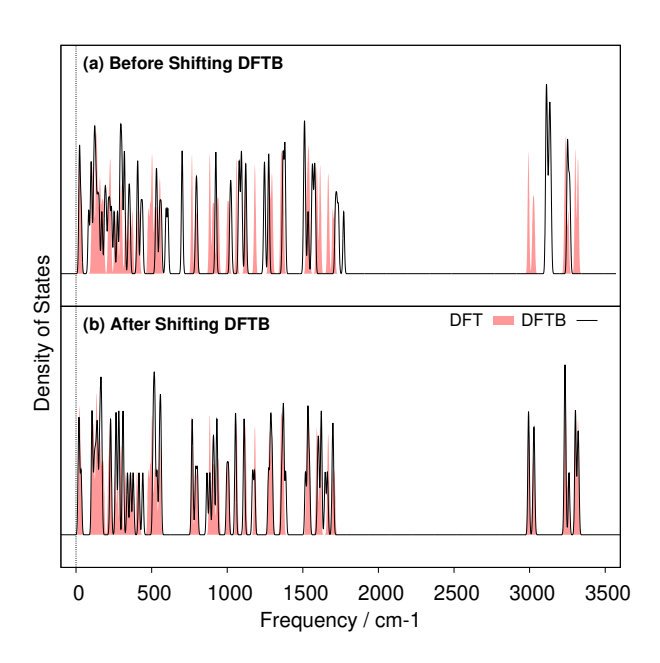


FIG. 4. Comparison of the DFTB3-D3(BJ) phonon density of states for the  $\alpha$  polymorph of oxalyl dihydrazide (a) before and (b) after the phonon shifting procedure against a supercell DFT (B86bPBE-XDM) calculation. The reference DFT pDOS is plotted in red, while the DFTB one is in black. All results except the unshifted DFTB pDOS in (a) include the corrected acoustic modes derived from DFT elastic constants.

impact the enthalpy and free energy via the zero-point vibrational energy. Close inspection of the pDOS in the low-frequency region also reveals discrepancies between the two models that will primarily impact the entropy as well as the temperature dependence of the enthalpy. In the region below  $500 \text{ cm}^{-1}$ , DFTB underestimates the DFT phonon frequencies by  $22 \text{ cm}^{-1}$  on average, or  $26 \text{ cm}^{-1}$  in mean absolute error.

Figure 4b shows how the pDOS is dramatically improved after shifting the DFTB phonon modes according to Eq 5 and correcting the acoustic modes. A few minor discrepancies do remain: for example, the shifted DFTB peaks near 500 cm<sup>-1</sup> should be broader and less intense, while the opposite is true for several peaks in the  $\sim$ 750–1750 cm<sup>-1</sup> range. Nevertheless, the shifted DFTB band positions and intensities as a whole exhibit far better agreement with the target DFT ones.

For more insight into the performance of the shifted DFT frequencies, Figure 5 plots the phonon frequencies for four modes in the 440–500 cm<sup>-1</sup> range for acetic acid. It shows how the additive shift, which ranges from 10–25 cm<sup>-1</sup> for these particular modes, brings

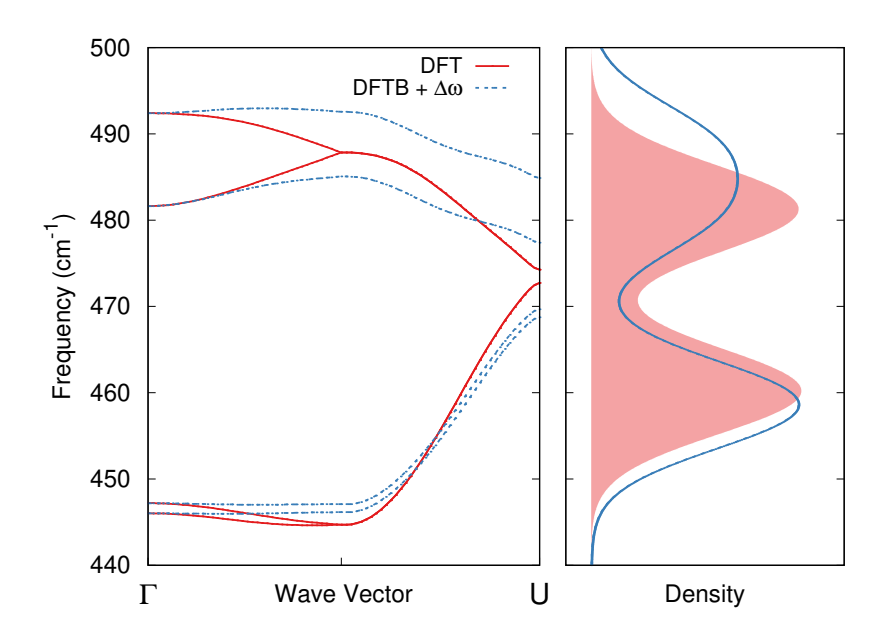


FIG. 5. A narrow region of the acetic acid phonon band structure (left) and density of states (right) as evaluated by DFT and DFTB after frequency shifting.

the DFTB phonon frequencies into perfect agreement with DFT at the  $\Gamma$ -point. However, the level of agreement between the two models is moderately reduced elsewhere in the Brillouin zone due to differences in the dispersion predicted by the two models. Nevertheless, the shifted DFTB pDOS still mimics the target DFT one fairly well, and it represents a noticeable improvement over the original, unshifted DFTB pDOS.

Next, we compare the performance of the approximate strategies for computing the room-temperature Helmholtz vibrational free energy against the DFT results obtained for acetic acid. Figure 6 plots the errors in the vibrational free energy per molecule relative what one obtains with supercell DFT (including elastic constant treatment of the acoustic modes). DFT Γ-point frequencies underestimate the target vibrational free energy by 2.5 kJ/mol compared to the supercell result. Given that the net vibrational free energy contribution to polymorph energy differences is often 1–2 kJ/mol, <sup>1,12</sup> this error is potentially significant.

DFTB Γ-point frequencies perform even worse, underestimating the target vibrational free energy by 6.8 kJ/mol. Including phonon dispersion via a supercell DFTB calculation further reduces the error by about a third, to 4.4 kJ/mol. Once the DFT-derived phonon frequency shift (Eq 5) is applied, however, the free energy error drops to 2.0 kJ/mol. Adding the appropriate acoustic modes (Eq 9) computed from the elastic constants brings the Helmholtz

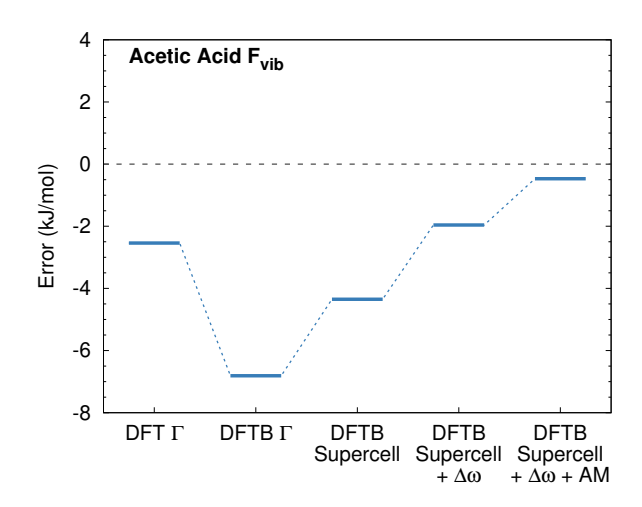


FIG. 6. Errors in the room-temperature Helmholtz vibrational free energies per molecule  $(F_{vib}(300K))$  computed with various approximate models relative to the full DFT supercell evaluation.

vibrational free energy to within 0.5 kJ/mol of the target supercell DFT treatment (which includes the same acoustic mode contributions).

Figure 7 plots the errors in the DFTB vibrational enthalpy, entropy (multiplied by temperature), and Helmholtz free energies for acetic acid as a function of temperature before and after applying the frequency shift and acoustic mode correction. Note that the pressure-volume work contribution to the enthalpy is negligible for a crystal at ambient pressure, which means that the Helmholtz and Gibbs free energies are essentially identical. Figure 7 highlights how the errors in the uncorrected DFTB model relative to the target DFT result vary considerably with temperature. For example, the errors in  $F_{vib}$  computed purely with DFTB range from -2.5 kJ/mol at 0 K to -4.3 kJ/mol at 300 K. The vibrational enthalpy error decreases with increasing temperature, from -2.5 kJ/mol to -1.8 kJ/mol, but this is more than compensated for by the growth of the error in the entropic contribution to the free energy. In contrast, after shifting the phonon frequencies and correcting the acoustic modes, the errors become much smaller and vary by only half a kJ/mol between 0 K and room temperature. The largest error in  $F_{vib}$  is only 0.5 kJ/mol, a nine-fold reduction from the uncorrected value.

For further insight, Table II examines the predicted thermochemical properties for five different crystals: carbon dioxide, acetic acid, imidazole, the  $\alpha$  polymorph of oxalyl dihy-

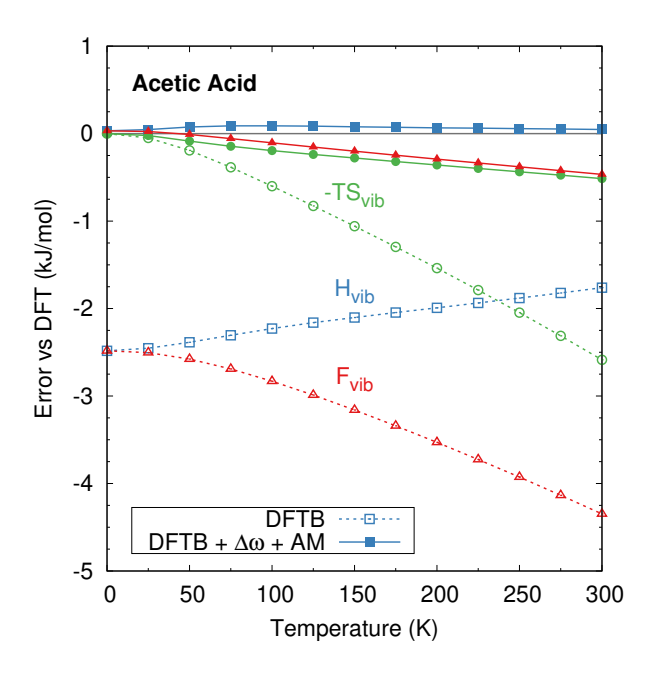


FIG. 7. Temperature-dependence of the errors in the predicted enthalpy (blue), entropic (green), and free energy (red) energies for crystalline acetic acid. Errors are computed relative to supercell DFT with the acoustic mode correction. Dotted lines correspond to the raw DFTB results, while solid lines indicate DFTB after shifting the frequencies and applying the acoustic mode fix.

drazide, and acetaminophen form I. Benchmark supercell DFT phonon calculations with acoustic mode corrections were performed for the three smaller crystals. Supercell DFT phonon calculations were not performed for oxalyl dihydrazide and acetaminophen due to computational expense.

For the first three crystals which have benchmark supercell DFT results, uncorrected DFTB exhibits modest mean absolute errors (MAD) in the vibrational enthalpy of 1.4 kJ/mol at 0 K and 1.2 kJ/mol at 300 K. In contrast, the frequency-shifted DFT models (with or without corrected acoustic modes) perform far better for the enthalpies, with a MAD of 0.1 kJ/mol. This MAD reflects a 0.4 kJ/mol error for carbon dioxide and essentially zero error for the other two crystals. Because the enthalpy is dominated by the zero-point contribution and exhibits modest temperature dependence, the frequency shift alone corrects most of the deficiencies of DFTB.

The vibrational entropy is more sensitive to the low-frequency phonon modes and shows greater variation across the different models. Raw DFTB performs poorly, with MAD of 4.7 kJ/mol in  $TS_{vib}$  at 300 K. This error reduces substantially to 1.3 kJ/mol upon shifting the

TABLE II. Predicted vibrational thermochemical contributions (excluding the electronic energy) for several molecular crystals, in kJ/mol per molecule, as computed with supercell DFTB, frequency-shifted supercell DFTB with corrected acoustic modes (AM), and supercell DFT with corrected acoustic modes.

	DFTB	DFTB	DFTB	DFT		
		$+\Delta\omega$	$+\Delta\omega{+}\mathrm{AM}$	+ AM		
Carbon Dioxide						
$H_{vib}(0\mathrm{K})$	30.4	32.4	32.5	32.0		
$H_{vib}(300\mathrm{K})$	42.4	43.3	43.3	43.1		
$TS_{vib}(300\mathrm{K})$	32.7	25.1	25.5	26.5		
$F_{vib}(300\mathrm{K})$	9.5	17.5	17.8	16.5		
Acetic Acid						
$H_{vib}(0\mathrm{K})$	160.7	163.2	163.2	163.2		
$H_{vib}(300\mathrm{K})$	175.5	177.3	177.3	177.3		
$TS_{vib}(300\mathrm{K})$	31.4	30.0	29.3	28.8		
$F_{vib}(300\mathrm{K})$	144.1	147.3	148.0	148.4		
	Imidazole					
$H_{vib}(0\mathrm{K})$	186.3	186.2	186.2	186.2		
$H_{vib}(300\mathrm{K})$	200.9	199.8	199.8	199.8		
$TS_{vib}(300\mathrm{K})$	34.5	30.5	30.0	29.2		
$F_{vib}(300\mathrm{K})$	166.3	169.2	169.7	170.6		
$\alpha$ -Oxalyl Dihydrazide						
$H_{vib}(0\mathrm{K})$	274.7	285.0	285.0	_		
$H_{vib}(300\mathrm{K})$	300.6	307.7	307.8	_		
$TS_{vib}(300\mathrm{K})$	52.2	45.5	43.5	_		
$F_{vib}(300\mathrm{K})$	248.4	262.2	264.3	_		
Acetaminophen Form I						
$H_{vib}(0\mathrm{K})$	411.4	414.7	414.7	_		
$H_{vib}(300\mathrm{K})$	442.0	444.3	444.3	-		
$TS_{vib}(300\mathrm{K})$	64.9	60.4	60.2	-		
$F_{vib}(300K)$	377.1	383.6	384.0	_		

frequencies and further down to 0.8 kJ/mol after correcting the acoustic modes. Because the errors for the two corrected DFTB models are dominated by the entropies, the errors in  $F_{vib}$  are similar. The final MAD error in the room-temperature free energies is 0.9 kJ/mol once the DFTB frequencies have been shifted and the acoustic modes corrected. Overall, the  $\sim$ 1 kJ/mol errors in the absolute vibrational free energies represent a several-fold improvement

over raw DFTB, and they are promising for organic crystal polymorphism problems for which some error cancellation often occurs when computing relative polymorph stabilities. The issue of error cancellation in relative polymorph free energies will be revisited below.

While benchmark DFT values were not obtained for oxalyl dihydrazide and acetaminophen, the data in Table II shows similar convergence behaviors of the different thermochemical quantities at the DFTB level. The frequency shift alters the DFTB enthalpies by up to 10 kJ/mol, while the acoustic mode correction has little impact. In contrast, both the frequency shift and acoustic mode corrections are important for the entropic contribution of oxalyl dihydrazide (and acetaminophen to a lesser extent). The final corrected free energies differ from the raw, uncorrected DFTB values by about 16 kJ/mol for oxalyl dihydrazide and 7 kJ/mol for acetaminophen. These errors are considerably larger than those found for the smaller three molecules discussed earlier, suggesting that the proposed DFTB corrections may become increasingly large as molecular complexity increases.

Next, we apply the pDOS approximation approach to the five polymorphs of oxalyl dihydrazide. This system is representative of polymorph problems where one might be interested in understanding how free energy contributions alter the relative polymorph stabilities. Oxalyl dihydrazide has five known polymorphs at ambient pressure, which are denoted  $\alpha$ ,  $\beta$ ,  $\gamma$ ,  $\delta$ , and  $\epsilon$ . Additional high-pressure forms have been reported, though they have not been fully characterized. The five ambient-pressure forms differ in their hydrogen bonding networks, including differences in whether they form intra- or intermolecular hydrogen bonds. The  $\beta$  polymorph is metastable and hard to crystallize; it is believed to be the least stable polymorph. The  $\gamma$  form is the second least stable. The  $\alpha$ ,  $\delta$ , and  $\epsilon$  forms are more stable than the other two, though the precise stability ordering among those three is unclear. Oxalyl dihydrazide has become a notable test case for electronic structure models due to its difficulty. A content of the following stability ordering (from most to least stable): )  $\alpha < \epsilon < \delta < \gamma < \beta$ , and this ordering will be taken as the correct one here.

Figure 8 compares the relative oxalyl dihydrazide polymorph stabilities as computed from pure B86bPBE-XDM electronic lattice energies ( $U_{el}$ ) and from several different Helmholtz vibrational free energy approximations. While the DFT electronic energy alone predicts the correct stability ordering, the 12 kJ/mol range is moderately larger than the 10 kJ/mol energy window that typically separates experimentally observed polymorphs.<sup>1–3</sup> The DFT  $\Gamma$ -

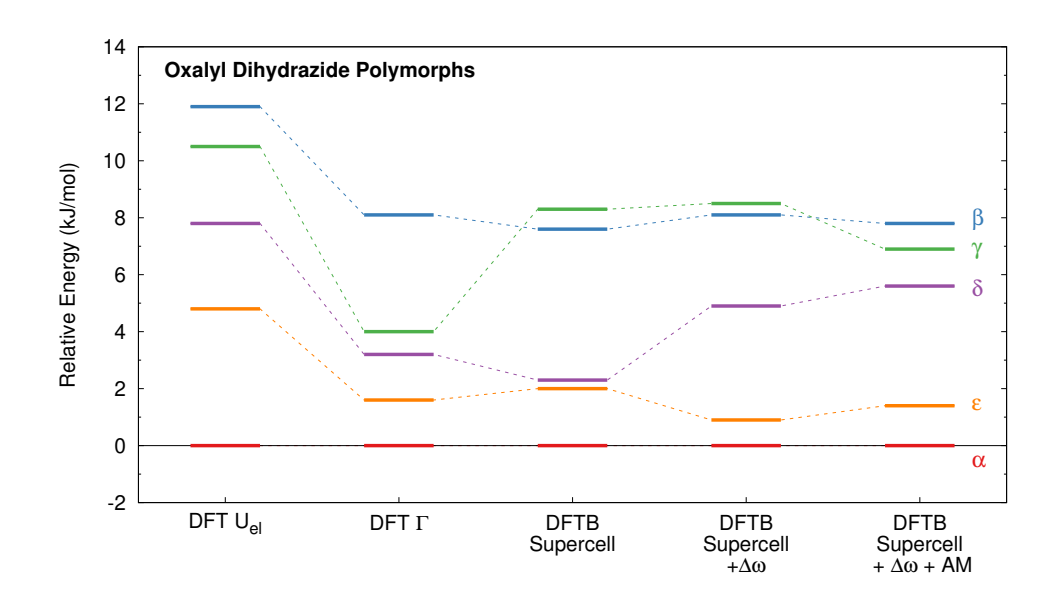


FIG. 8. Relative stabilities of the five oxalyl dihydrazide polymorphs. The first column presents relative DFT electronic lattice energies, while the subsequent ones correspond to free energies as computed from  $\Gamma$ -point DFT frequencies, supercell DFTB, and supercell DFTB corrected with the frequency shift and acoustic modes.

point approximation to the free energy narrows this range somewhat, stabilizing the  $\gamma$  form most noticeably. Using the raw DFTB supercell phonon treatment alters the stabilities considerably, and it incorrectly suggests that the  $\gamma$  form is less stable than the  $\beta$  one. Not until both the  $\Gamma$ -point frequency shift and the acoustic mode correction are included do the free energies predict a stability ordering that is consistent with experiment. Without further experimental information, it is not possible to assess the quantitative accuracy of these stabilities, but it is reassuring to see that the proposed approximations for the phonon density of states does produce the qualitatively correct polymorph rankings in this difficult system.

It is also worth noting how the differences in the relative polymorph free energies vary by only a few kJ/mol between models, while the absolute  $F_{vib}$  values in for  $\alpha$  oxalyl dihydrazide in Table II differ by 16 kJ/mol between the corrected and uncorrected DFTB results. In other words, considerable error cancellation occurs in the relative polymorph free energies. Despite the error cancellation, the uncorrected DFTB results predict qualitatively incorrect relative free energies. This emphasizes the importance of the DFTB correction for capturing the small energy differences associated with polymorphism.

TABLE III. Computational cost associated with computing the different phonon density of states approximations for acetic acid, computed relative to the cost of a DFT  $\Gamma$ -point frequency evaluation. The relative costs were derived from processor hours, rather than wall time.

Model	Relative Cost
DFT Γ	1.0
DFTB $\Gamma$	0.02
DFTB Supercell	18.6
Shifted DFTB Supercell	19.6
Shifted DFTB Supercell + Acoustic Modes	22.9
DFT Supercell	614.6
DFT Supercell + Acoustic Modes	617.8

Finally, we examine the computational savings associated with the approximate pDOS treatment explored here. Table III summarizes the relative computational costs associated with evaluating the acetic acid pDOS. The  $2\times4\times3$  supercell used here contains 24 replicas of the crystallographic unit cell, for a total of 768 atoms. The cost of the DFTB supercell phonon calculation is about 19 times that of a DFT  $\Gamma$ -point one. On the other hand, that is far cheaper than the supercell DFT calculation, which costs 615 times that of the DFT  $\Gamma$ -point one. The fixed-cell geometry optimizations required to evaluate the elastic constants and acoustic modes have an effective cost of about three times the DFT  $\Gamma$ -point frequency calculation for this system. In other words, the additional calculations required to perform the pDOS correction comprise only a small fraction of the DFTB supercell phonon calculation. Combining the DFT  $\Gamma$ -point calculation, the DFTB supercell one, and acoustic mode correction brings the total computational cost to 22.9 times that of the DFT  $\Gamma$ -point alone. This is 27 times faster than the supercell DFT calculation (including the acoustic mode correction), with only 0.4 kJ/mol loss in accuracy in the vibrational free energy at room temperature (cf Table II).

## V. CONCLUSIONS

Despite its computational efficiency advantages, the phonon density of states computed from DFTB3-D3(BJ) with the 3ob-3-1 parameterization exhibits appreciable errors relative to a DFT GGA treatment. In the systems examined here, these discrepancies introduce errors ranging from a few kJ/mol to more than ten kJ/mol. Even with the error cancellations that can occur in relative energies, it seems likely that thermochemical properties predicted from this DFTB model will be unable to provide the kJ/mol accuracy often required for problems in organic polymorphism and crystal structure prediction.

This study demonstrated how a simple additive shift to the DFTB phonon frequencies and careful treatment of the acoustic modes leads to a model that performs far better with only moderate increase in computational cost. Unsurprisingly, the biggest improvements from the corrections manifest in the entropic contribution to the free energy, since that term is particularly sensitive to the low-frequency phonon modes. However, sizable corrections were found for the absolute vibrational enthalpies as well, arising primarily from the zero-point contribution.

The correction proposed in this study is independent from the particular DFTB approximation or density functional used here. The same ideas could be applied to any pair of "high" and "low" level models. Improvements to existing DFTB models and parameterizations that are actively being pursued by the community could be useful in this context, including extensions to hybrid and/or range-separated functionals and better descriptions of non-covalent interactions. Alternatively, semi-empirical composite models have found success in non-covalent interactions and certain aspects of crystal structure prediction 45,47,74–76 and could potentially be suitable here too. The most important criteria in selecting the appropriate pair of models will be the accuracy of the high-level method, the computational cost of the two methods, and the fidelity with which the low-level method reproduces the shapes of the phonon dispersion curves. In the future, it will be interesting to employ this approach more widely. Beyond basic harmonic free energy contributions, the approach could readily be combined with quasi-harmonic calculations of phase diagrams, spectroscopic properties, mechanical properties, etc.

## **ACKNOWLEDGMENTS**

Funding for this work from the National Science Foundation (CHE-1955554) and supercomputer time from XSEDE (TG-CHE110064) are gratefully acknowledged.

# DATA AVAILABILITY

The data that support the findings of this study are available from the corresponding author upon reasonable request.

## REFERENCES

- <sup>1</sup>J. Nyman and G. M. Day, CrystEngComm 17, 5154 (2015).
- <sup>2</sup>A. J. Cruz-Cabeza, S. M. Reutzel-Edens, and J. Bernstein, Chem. Soc. Rev. **44**, 8619 (2015).
- $^3\mathrm{A.}$  Burger and R. Ramberger, Mikrochim. Acta $\mathbf{72},\,273$  (1979).
- <sup>4</sup>G. J. O. Beran, J. D. Hartman, and Y. N. Heit, Acc. Chem. Res. **49**, 2501 (2016).
- $^{5}$ G. J. O. Beran, Chem. Rev. **116**, 5567 (2016).
- <sup>6</sup>S. R. Whittleton, A. Otero-de-la Roza, and E. R. Johnson, J. Chem. Theory Comput. **13**, 441 (2017).
- <sup>7</sup>J. Hoja, H.-Y. Ko, M. A. Neumann, R. Car, R. A. DiStasio, and A. Tkatchenko, Science Adv. 5, eaau3338 (2019).
- <sup>8</sup>C. Greenwell, J. L. McKinley, P. Zhang, Q. Zeng, G. Sun, B. Li, S. Wen, and G. J. O. Beran, Chem. Sci. **11**, 2200 (2020).
- <sup>9</sup>C. Greenwell and G. J. O. Beran, Cryst. Growth Des. **20**, 4875 (2020).
- <sup>10</sup>A. Gavezzotti and G. Filippini, Journal of the American Chemical Society 117, 12299 (1995).
- <sup>11</sup>S. L. Price, Chem. Soc. Rev. **43**, 2098 (2014).
- $^{12}\mathrm{J}.$  Nyman and G. M. Day, Phys. Chem. Chem. Phys.  $\mathbf{18},\,31132$  (2016).
- $^{13}\mathrm{A.~M.}$  Reilly and A. Tkatchenko, Phys. Rev. Lett.  $\boldsymbol{113},\,055701$  (2014).
- <sup>14</sup>A. Erba, J. Maul, and B. Civalleri, Chem. Commun. **52**, 1820 (2016).
- <sup>15</sup>Y. N. Heit and G. J. O. Beran, Acta Cryst. B **72**, 514 (2016).
- <sup>16</sup>J. Hoja, A. M. Reilly, and A. Tkatchenko, WIREs Comput. Mol. Sci. 7, e1294 (2017).

- <sup>17</sup>C. Červinka, M. Fulem, R. P. Stoffel, and R. Dronskowski, J. Phys. Chem. A **120**, 2022 (2016).
- <sup>18</sup>C. Červinka and M. Fulem, J. Chem. Theory Comput. **13**, 2840 (2017).
- <sup>19</sup>C. Červinka and G. J. O. Beran, Phys. Chem. Chem. Phys. **19**, 29940 (2017).
- <sup>20</sup>C. Červinka and G. J. O. Beran, Chem. Sci. **9**, 4622 (2018).
- <sup>21</sup>C. Červinka and G. J. O. Beran, Phys. Chem. Chem. Phys. **21**, 14799 (2019).
- <sup>22</sup>Y. N. Heit, K. D. Nanda, and G. J. O. Beran, Chem. Sci. 7, 246 (2016).
- <sup>23</sup>M. A. Salim, S. Y. Willow, and S. Hirata, J. Chem. Phys. **144**, 204503 (2016).
- <sup>24</sup>M. T. Ruggiero, J. A. Zeitler, and A. Erba, Chemical Communications **53**, 3781 (2017).
- <sup>25</sup>W. Sontising, Y. N. Heit, J. L. McKinley, and G. J. O. Beran, Chem. Sci. 8, 7374 (2017).
- <sup>26</sup>J. L. McKinley and G. J. O. Beran, J. Chem. Theory Comput. **15**, 5259 (2019).
- <sup>27</sup>E. C. Dybeck, N. S. Abraham, N. P. Schieber, and M. R. Shirts, Cryst. Growth Des. 17, 1775 (2017).
- <sup>28</sup>N. P. Schieber, E. C. Dybeck, and M. R. Shirts, J. Chem. Phys. **148**, 144104 (2018), arXiv:1711.00979.
- <sup>29</sup>E. C. Dybeck, D. P. McMahon, G. M. Day, and M. R. Shirts, Cryst. Growth Des. 19, 5568 (2019).
- <sup>30</sup>N. S. Abraham and M. R. Shirts, Cryst. Growth Des. **19**, 6911 (2019).
- <sup>31</sup>M. Born and K. Huang, *Dynamical Theory of Crystal Lattices* (Clarendon Press, 1954).
- $^{32}{\rm A.~M.}$  Reilly and A. Tkatchenko, J. Chem. Phys.  ${\bf 139},\,024705$  (2013).
- $^{33}\mathrm{J}.$  Hoja and A. Tkatchenko, Faraday Disc.  $\mathbf{211},\,253$  (2018), arXiv:arXiv:1803.07503.
- <sup>34</sup>S. Baroni, S. de Gironcoli, A. Dal Corso, and P. Giannozzi, Rev. Mod. Phys. **73**, 516 (2001).
- $^{35}\mathrm{J}.$  L. McKinley and G. J. O. Beran, Faraday Disc.  $\mathbf{211},\,181$  (2018).
- $^{36}\mathrm{M}.$  Elstner and G. Seifert, Philos. Trans. Roy. Soc. A  $\mathbf{372},\,20120483$  (2014).
- <sup>37</sup>A. S. Christensen, T. Kubař, Q. Cui, and M. Elstner, Chem. Rev. **116**, 5301 (2016).
- <sup>38</sup>M. Gaus, Q. Cui, and M. Elstner, J. Chem. Theory Comput. **7**, 931 (2011).
- <sup>39</sup>S. Grimme, J. Antony, S. Ehrlich, and H. Krieg, J. Chem. Phys. **132**, 154104 (2010).
- $^{40}\mathrm{J}.$  Řezáč, J. Chem. Theory Comput. 13, 4804 (2017).
- <sup>41</sup>M. Mortazavi, J. G. Brandenburg, R. J. Maurer, and A. Tkatchenko, J. Phys. Chem. Lett. **9**, 399 (2018).

- <sup>42</sup>J. G. Brandenburg, J. Potticary, H. A. Sparkes, S. L. Price, and S. R. Hall, J. Phys. Chem. Lett. 8, 4319 (2017).
- <sup>43</sup>L. Iuzzolino, P. McCabe, S. L. Price, and J. G. Brandenburg, Faraday Disc. **211**, 275 (2018).
- <sup>44</sup>G. A. Dolgonos, O. A. Loboda, and A. D. Boese, J. Phys. Chem. A **122**, 708 (2018).
- <sup>45</sup>J. G. Brandenburg, M. Hochheim, T. Bredow, and S. Grimme, J. Phys. Chem. Lett. **5**, 4275 (2014).
- <sup>46</sup>J. G. Brandenburg and S. Grimme, J. Phys. Chem. Lett. **5**, 1785 (2014).
- <sup>47</sup>J. G. Brandenburg, T. Maas, and S. Grimme, J. Chem. Phys. **142**, 124104 (2015).
- <sup>48</sup>J. G. Brandenburg and S. Grimme, Acta Cryst. B **72**, 502 (2016).
- <sup>49</sup>M. Dove, Collection SFN **12**, 123 (2011).
- <sup>50</sup>D. Alfe, Comput. Phys. Comm. **180**, 2622 (2009).
- <sup>51</sup>M. Gaus, A. Goez, and M. Elstner, J. Chem. Theory Comput. 9, 338 (2013).
- <sup>52</sup>M. Musgrave, *Crystal Acoustics* (Holden-Day, 1970).
- $^{53}$ J. Reissland, *The Physics of Phonons* (John Wiley & Sons, 1973).
- <sup>54</sup>J. Nyman, O. Sheehan Pundyke, and G. M. Day, Phys. Chem. Chem. Phys. **18**, 15828 (2016).
- <sup>55</sup>W. H. Keesom and J. W. Köhler, Physica **1**, 655 (1934).
- $^{56}\mathrm{I.}$  Nahringbauer, Acta Chem. Scand. A  $\mathbf{24},\,453$  (1970).
- <sup>57</sup>R. K. McMullan, J. Epstein, J. R. Ruble, and B. M. Craven, Acta Cryst. B **35**, 688 (1979).
- <sup>58</sup>M. Haisa, S. Kashino, R. Kawai, and H. Maeda, Acta Cryst. B **32**, 1283 (1976).
- <sup>59</sup>S. Ahn, F. Guo, B. M. Kariuki, and K. D. M. Harris, J. Am. Chem. Soc. **128**, 8441 (2006).
- <sup>60</sup>P. Giannozzi, S. Baroni, N. Bonini, M. Calandra, R. Car, C. Cavazzoni, D. Ceresoli, G. L. Chiarotti, M. Cococcioni, I. Dabo, A. Dal Corso, S. de Gironcoli, S. Fabris, G. Fratesi, R. Gebauer, U. Gerstmann, C. Gougoussis, A. Kokalj, M. Lazzeri, L. Martin-Samos, N. Marzari, F. Mauri, R. Mazzarello, S. Paolini, A. Pasquarello, L. Paulatto, C. Sbraccia, S. Scandolo, G. Sclauzero, A. P. Seitsonen, A. Smogunov, P. Umari, and R. M. Wentzcovitch, J. Phys. Condens. Mat. 21, 395502 (2009).
- <sup>61</sup>B. Aradi, B. Hourahine, and T. Frauenheim, Journal of Physical Chemistry A **111**, 5678 (2007).

- <sup>62</sup>B. Hourahine, B. Aradi, V. Blum, F. Bonafé, A. Buccheri, C. Camacho, C. Cevallos, M. Y. Deshaye, T. Dumitrică, A. Dominguez, S. Ehlert, M. Elstner, T. van der Heide, J. Hermann, S. Irle, J. J. Kranz, C. Köhler, T. Kowalczyk, T. Kubař, I. S. Lee, V. Lutsker, R. J. Maurer, S. K. Min, I. Mitchell, C. Negre, T. A. Niehaus, A. M. N. Niklasson, A. J. Page, A. Pecchia, G. Penazzi, M. P. Persson, J. Řezáč, C. G. Sánchez, M. Sternberg, M. Stöhr, F. Stuckenberg, A. Tkatchenko, V. W. Yu, and T. Frauenheim, J. Chem. Phys. 152, 124101 (2020).
- $^{63}\mathrm{A}.$  Otero-de-la Roza and E. R. Johnson, J. Chem. Phys.  $\mathbf{136},\,174109$  (2012).
- <sup>64</sup>A. Otero-De-La-Roza, B. H. Cao, I. K. Price, J. E. Hein, and E. R. Johnson, Angew. Chem. Int. Ed. **53**, 7879 (2014).
- <sup>65</sup>S. R. Whittleton, A. Otero-de-la Roza, and E. R. Johnson, J. Chem. Theory Comput. 13, 5332 (2017).
- <sup>66</sup>A. Otero-de-la Roza, L. M. LeBlanc, and E. R. Johnson, J. Chem. Theory Comput. 15, 4933 (2019).
- $^{67}\mathrm{A}.$  Togo and I. Tanaka, Scripta Materialia  $\mathbf{108},\,1$  (2015).
- <sup>68</sup>W. Setyawan and S. Curtarolo, Comput. Mater. Sci. **49**, 299 (2010), arXiv:1004.2974.
- <sup>69</sup>D. Corso, Thermo\_pw, https://dalcorso.github.io/thermo\_pw.
- <sup>70</sup>X. Tan, K. Wang, T. Yan, X. Li, J. Liu, K. Yang, B. Liu, G. Zou, and B. Zou, J. Phys. Chem. C 119, 10178 (2015).
- <sup>71</sup>P. G. Karamertzanis, G. M. Day, G. W. A. Welch, J. Kendrick, F. J. J. Leusen, M. A. Neumann, and S. L. Price, J. Chem. Phys. **128**, 244708 (2008).
- <sup>72</sup>S. Wen and G. J. O. Beran, J. Chem. Theory Comput. **8**, 2698 (2012).
- <sup>73</sup>D. Presti, A. Pedone, M. C. Menziani, B. Civalleri, and L. Maschio, CrystEngComm 16, 102 (2014).
- <sup>74</sup>S. Grimme, C. Bannwarth, and P. Shushkov, J. Chem. Theory Comput. 13, 1989 (2017).
- <sup>75</sup>J. G. Brandenburg, C. Bannwarth, A. Hansen, and S. Grimme, J. Chem. Phys. **148**, 064104 (2018).
- $^{76}\mathrm{L}.$  M. LeBlanc and E. R. Johnson, CrystEngComm  $\mathbf{21},\,5995$  (2019).